TRANSPORT PHENOMENA AND FLUID MECHANICS

AIChE JOURNAL

Droplet impingement and wetting behavior on a chemically heterogeneous surface in the Beyond–Cassie–Baxter regime

Guina Yi[1,2] | **Ziqi Cai**[1,2,3] | **Zhengming Gao**[1,2] | **Zhichao Jiang**[4] |
Xiongbin Huang[1,2] | **Jos J. Derksen**[5] 🔵

[1]Beijing Advanced Innovation Center for Soft Matter Science and Engineering, Beijing University of Chemical Technology, Beijing, China

[2]State Key Laboratory of Chemical Resource Engineering, School of Chemical Engineering, Beijing University of Chemical Technology, Beijing, China

[3]Department of Chemical Science and Engineering, Kobe University, Kobe, Hyogo, Japan

[4]Research Institute of Petroleum Processing, SINOPEC, Beijing, China

[5]School of Engineering, University of Aberdeen, Aberdeen, UK

Correspondence
Ziqi Cai and Zhengming Gao, Beijing Advanced Innovation Center for Soft Matter Science and Engineering, Beijing University of Chemical Technology, Beijing 100029, China.
Email: caiziqi@mail.buct.edu.cn (Z. C.) and gaozm@mail.buct.edu.cn (Z. G.)

Abstract

Droplet impingement and anisotropic wetting on chemically heterogeneous stripe-patterned surfaces is simulated by means of many-body dissipative particle dynamics. The ratio of the stripe width and initial droplet diameter, defined as β, ranges from 0.5 to 1.0 so that the wetting process is in the Beyond–Cassie–Baxter regime and is highly anisotropic. At zero Weber number (that is, without considering droplet inertia) and with superhydrophobic stripes, β is the only factor affecting the droplet perpendicular contact angle and aspect ratio. For inertial droplets, β and the Weber number are found to have an effect on the eventual droplet morphology on multi-striped surfaces. These morphologies include elongated shape, split-off, and "butterfly" shape. A correlation for critical split-off conditions has been determined. An energy analysis of droplet impingement shows that the normalized surface energy of the droplet is independent of the Weber number if the droplet is elongated or butterfly-shaped.

KEYWORDS

anisotropic wetting, droplet evolution, droplet impingement, many-body dissipative particle dynamics, surface energy

1 | INTRODUCTION

Anisotropic wetting of a droplet on grooved surfaces[1,2] and chemically heterogeneous surfaces[3-7] is commonly observed in nature[3] and industrial applications, such as ink jet printing,[4] microfluidics systems,[5] droplet evaporation[6] and cell culture.[7] Different from wetting on homogeneous surfaces, the droplet morphology will adapt to the alternations of wettability on the chemically heterogeneous surface, and the droplet's final shape strongly depends on the topology of wettability of the surface. Various chemically heterogeneous surfaces such as stripes,[8-10] square,[11,12] and triangular patterns[13] have been investigated. Striped surfaces get a lot of attention due to their relatively easy fabrication. When a droplet deposits on a striped surface slowly, the contact angles of the droplet in the directions perpendicular ($\theta_\perp$) and parallel ($\theta_\parallel$) to the stripes can be very different, as shown in Figure 1.

The aspect ratio, W/L as shown in Figure 1, is used to describe the droplet deformation, where W is the width of the droplet perpendicular to the stripes and L is the length of the droplet parallel to the stripes. Relative hydrophobicity of the stripes is described as $\alpha = \frac{W_{bic}}{W_{lic}}$, where W_{bic} and W_{lic} are the width of hydrophobic and hydrophilic stripe, respectively.[14] Much research has been done for droplet sizes much larger than the stripe width so that the droplet covers multiple stripes simultaneously, typically more than ten.[15] Bliznyuk et al[14,16]
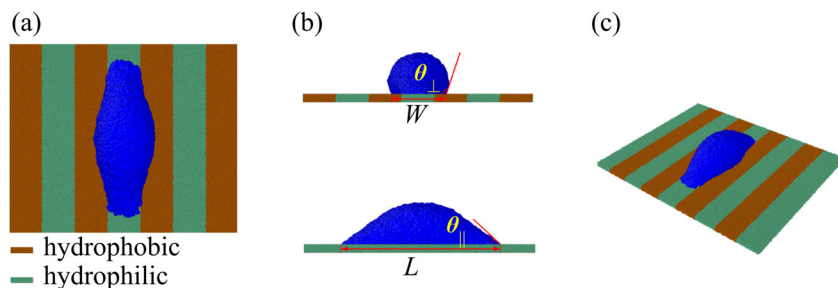
FIGURE 1 Schematic representation of a droplet on a chemically stripe-patterned surface: (a) Top view. (b) Front and side view. W and L represent the droplet width and length, respectively. $\theta_\perp$ and $\theta_\parallel$ represent contact angles perpendicular and parallel to the direction of the stripes, respectively. (c) perspective view [Color figure can be viewed at wileyonlinelibrary.com]

deposited glycerol droplets of millimeter size on alternating hydrophilic and hydrophobic stripes to investigate the final shape of the droplet. Two spreading regimes[16] were observed during the droplet deposition. At the beginning of the deposition, droplet spreading is in the inertial regime, where the spreading rate of the droplet in both perpendicular and parallel direction are the same. Subsequently, the droplet is elongated in the viscous regime, where the droplet spreads more along the stripe because of the energy barrier in the perpendicular direction. In addition, they noticed that the contact angles and aspect ratio of the equilibrium droplet only depend on α if the size of the droplet is one to two orders of magnitude larger than the width of the stripes.[14] The experiment[14] was later compared with the simulations conducted by Jansen et al[17] based on a finite element method. Both the experiments and simulations indicated a more elongated droplet on the surface with low α. Additionally, $\theta_\perp$ is close to the intrinsic contact angle of the hydrophobic stripes (θ_{bic}) for a large α range, and $\theta_\parallel$ can be modeled by the Cassie–Baxter equation[14]: $\theta_\parallel = \arccos\left[\frac{\alpha\cos(\theta_{\text{bic}}) + \cos(\theta_{\text{lic}})}{1 + \alpha}\right]$, where θ_{lic} is the intrinsic contact angle of the hydrophilic stripes. The equation indicates that the morphology of a droplet in the Cassie–Baxter regime can be adjusted by modifying θ_{bic}, θ_{lic}, and α.

Different from a droplet spanning multiple stripes, when the stripe width is comparable with the initial droplet radius, the contact angles of the droplet cannot be predicted by the Cassie–Baxter equation anymore.[18] Wang et al[18] suggested 0.1 as the critical value for the ratio of stripe width to droplet radius that separates the Cassie–Baxter regime and the Beyond–Cassie–Baxter regime. In the Beyond–Cassie–Baxter regime, the equilibrium shape of the droplet is related to the number of wetted stripes and the initial deposition position. Jansen et al[19] defined a scaled radius to describe the relative size of the droplet and the stripes. They performed lattice-Boltzmann simulations to model droplet wetting on striped surfaces with the scaled radius ranging from 0.5 to 1.25. Interestingly, $\theta_\perp$ and the aspect ratio of the droplet do not change monotonically as the scaled radius increases. Instead, they firstly increase until they undergo a sudden transition where a minimum occurs and then they start a new stage of increase. If the number of wetted stripes reduces to three, "lozenge" and "butterfly" shapes are identified when a droplet is deposited on the middle of a hydrophobic and hydrophilic stripe, respectively.[18,20] Lipowsky et al[21,22] observed four morphologies on a single hydrophilic stripe, where a long liquid channel could be obtained by adding more and more liquid onto a stripe with wettability if $\theta_{\text{lic}} < 38°$.

When the initial velocity of the droplet is significant, the effects of its inertia on the impinging and wetting process cannot be ignored. The impinging dynamics is characterized by the droplet Weber number ($We = \frac{\rho U^2 D_0}{\sigma}$), which is the ratio of inertial force to capillary force. Here, U is the impinging velocity; ρ, σ and D_0 are the density, surface tension and initial diameter of the spherical droplet, respectively. Song et al[23] found that the droplet could be split off by impinging it on a slim superhydrophobic stripe coating placed on a hydrophilic surface if $We > 20$. In the case of multiple stripes, Zhao et al[24] conducted a 2D simulation based on many-body dissipative particle dynamics (MDPD) to study the droplet impingement on a multi-striped surface, and they observed "stick–slip" motion of the droplet during the recoiling stage, which was strongly affected by We and α. Jansen et al[8,25] pointed out that more spherical droplets could be obtained in higher We cases. With increasing We, there may be some residues or satellite droplet on hydrophilic stripes. Wang et al[26] found that these residues were distributed in circular regions. Zou et al[27] indicated that the number of satellite droplets increases with increasing droplet impinging velocity, that is, with increasing We.

Despite that much work has been performed on the droplet impingement on stripe pattern surfaces, there is no clear understanding of the droplet spreading and impingement behavior in the Beyond–Cassie–Baxter regime. In this regime, the droplet can be deformed, migrate and even be split into two droplets, dependent on stripes width and wettability. The aim of this work is to investigate the droplet behavior in the Beyond–Cassie–Baxter regime characterized by droplet spreading diameters, contact angles, aspect ratios and droplet energy budgets. In this work, the relative stripe width, β, defined by the ratio between the stripe width W_s and initial droplet diameter D_0, ranges from 0.5 to 1.0. The hydrophilic contact angle has been fixed at 45° and hydrophobic contact angle is variable.

Here we use MDPD to investigate single droplet impingement and wetting behavior. MDPD is a mesoscopic numerical method that has been widely employed in multi-fluid systems with free liquid/vapor or liquid/liquid interfaces, such as capillary flow,[28] liquid droplets on surfaces,[29-31] and bubble formation.[32] All the simulations in this work are implemented by a modified MDPD code in the open source molecular dynamics code LAMMPS (Large-scale Atomic/Molecular Massively Parallel Simulator).[33]

The remainder of the paper is organized along the following lines: a brief introduction about the MDPD method and validation tests are presented in Section 2, and then the results are shown in Section 3.

Firstly, we discuss wetting without taking into account inertial effect. We analyze the effects of deposition position and the hydrophobic stripes wettability on the droplet shape. Next, the droplet impingement behavior including inertial effects is discussed. The effects of the stripe arrangement, β and We on droplet morphology are investigated. In addition, the time evolution of droplet surface energy and kinetic energy are introduced to describe the droplet impingement behavior. A final section summarizes the main conclusions and makes suggestions for future work.

2 | NUMERICAL METHOD

2.1 | MDPD method

The MDPD method, a mesoscopic numerical method, is derived from dissipative particle dynamics (DPD).[34-36] As is the case for the standard DPD method, each particle in MDPD represents a cluster of atoms or molecules and the motion of each particle obeys Newton's second law, where the total force acting on each particle includes conservative force $\mathbf{F}_{ij}^{C}$, dissipative force $\mathbf{F}_{ij}^{D}$ and random force $\mathbf{F}_{ij}^{R}$. Different from standard DPD, an attractive term is introduced in MDPD to simulate vapor–liquid coexistence. For this reason, the conservative force ($\mathbf{F}_{ij}^{C}$) in MDPD is defined as:

$$\mathbf{F}_{ij}^{C} = \left[A_{ij} w_{C}\left(r_{ij}\right) + B_{ij}\left(\bar{\rho}_{i} + \bar{\rho}_{j}\right) w_{d}\left(r_{ij}\right) \right] \mathbf{e}_{ij} \tag{1}$$

Here, A_{ij}, usually negative, is the coefficient of the attractive force between particle i and particle j within a cutoff range r_{C}; B_{ij}, usually greater than zero, is the density-dependent repulsive force coefficient within a cutoff range r_{d}. The weight functions are $w_{C}(r_{ij}) = 1 - r_{ij}/r_{C}$ and $w_{d}(r_{ij}) = 1 - r_{ij}/r_{d}$ with r_{ij} the distance between particle i and particle j, and $\mathbf{e}_{ij}$ is the unit vector from particle j to i. The local density ρ at the location of particle i can be obtained by $\bar{\rho}_{i} = \sum_{j \neq i} w_{\rho}\left(r_{ij}\right)$ where $w_{\rho}\left(r_{ij}\right) = \frac{15}{2\pi r_{d}^{3}}\left(1 - \frac{r_{ij}}{r_{d}}\right)^{2}$, according to References 34 and 37.

Apart from the conservative force, the other components in the total force are the same as those in standard DPD. They can be written as:

$$\mathbf{F}_{ij}^{D} = -\gamma w_{D}\left(r_{ij}\right)\left(\mathbf{e}_{ij} \cdot \mathbf{v}_{ij}\right)\mathbf{e}_{ij} \tag{2}$$

$$\mathbf{F}_{ij}^{R} = \delta w_{R}\left(r_{ij}\right)\xi_{ij}\Delta t^{-1/2}\mathbf{e}_{ij} \tag{3}$$

where γ and δ are the friction coefficient and the noise amplitude, respectively; w_{D} and w_{R} are weight functions; $\mathbf{v}_{ij} = \mathbf{v}_{i} - \mathbf{v}_{j}$ is the relative velocity between particle i and particle j; ξ_{ij} is a random Gaussian number with zero mean and unit variance. To satisfy the fluctuation-dissipation theorem requires that $\delta^{2} = 2\gamma k_{B}T$ and $w_{D}(r_{ij}) = [w_{R}(r_{ij})]^{2}$, where k_{B} is the Boltzmann constant and T is the system temperature. The weight function for dissipative force and random force are $w_{R}(r_{ij}) = 1 - r_{ij}/r_{C}$, and $w_{D}(r_{ij}) = (1 - r_{ij}/r_{C})^{2}$, respectively.[38]

2.2 | Fluid properties and validation

In this section, we test the MDPD method by comparing our simulation results of a droplet spreading on a solid surface with the corresponding experimental results in Reference 39 Generally, MDPD operates in reduced units so that $k_{B}T = 1.0$ and $r_{C} = 1.0$. A common choice for the interaction parameters between liquid particles then is $A_{ll} = -40$, $B_{ll} = 25$ and $r_{d} = 0.75$.[13,28,37]

Figure 2a shows the density profile of a spherical droplet with the density of the droplet $\rho = 6.09$, which is slightly different from $\rho = 6.0$ as obtained in Reference 28 with exactly the same set of parameters. Surface tension is an important interface property in the interaction between a liquid droplet and a solid surface. Conducting a simulation of a thin liquid film, the surface tension can be derived by subtracting the mean tangential stress components (i.e., P_{xx} and P_{yy}) from the normal (i.e., P_{zz}): $\sigma = \int_{-\infty}^{\infty} dz\left[P_{zz} - \frac{1}{2}\left(P_{xx} + P_{yy}\right)\right]$.[40] The calculated surface tension is $\sigma = 7.51$, which matches the value in Reference 28($\sigma = 7.51 \pm 0.04$).

The viscosity of the liquid can be assessed separately from ρ and σ and directly obtained by the periodic Poiseuille flow method.[37,41,42] In this validation, the parameter γ equals 0.005. A computational box filled with 4,677 particles is divided into two symmetric regions and a body force along the z direction is applied to each particle located in a half of the box, while an equal force in the opposite direction is applied to particles in the other half. This distribution of forces leads to parabolic velocity profiles on either side of the box, as seen in Figure 2b. Fitting the simulated time-averaged velocity in z-direction as a function of x with a quadratic function—as shown in Figure 2b—then provides us with an estimate for the kinematic viscosity of $\upsilon = 0.40$.

The relationship between the MDPD units of length (L_{MDPD}), mass (M_{MDPD}) and time (T_{MDPD}) can be mapped to specific properties of real liquids (i.e., density ρ^{*}, surface tension σ^{*} and viscosity υ^{*}) according to Equation (4).[37]

$$
\begin{aligned}
M_{MDPD} &= L_{MDPD}^{3}\frac{\rho^{*}}{\rho} \\
T_{MDPD} &= \left(M_{MDPD}\frac{\sigma}{\sigma^{*}}\right)^{0.5} \\
\frac{L_{MDPD}^{2}}{T_{MDPD}} &= \frac{\upsilon^{*}}{\upsilon}
\end{aligned} \tag{4}
$$

As an example, the ethylene glycol solution as used in Reference 39 ($\rho^{*} = 1{,}056$ kg/m^3, $\sigma^{*} = 56.5$ mN/m and $\upsilon^{*} = 3.03 \times 10^{-6}$ m^2/s) can be matched by $\rho = 6.09$, $\sigma = 7.51$ and $\upsilon = 0.4$, respectively. So we determine the scaling coefficients between the physical and MDPD units as $L_{MDPD} = 1.32 \times 10^{-6}$ m, $M_{MDPD} = 4.01 \times 10^{-16}$ kg, and $T_{MDPD} = 2.31 \times 10^{-7}$ s by Equation (4).

Droplets with different static contact angle (θ_{c}) on the substrate can be created by altering the solid–liquid interaction parameter A_{sl}. The relationship between A_{sl} and θ_{c} is shown in Figure 2c. The range of A_{sl} is from -37 to -4 and the range of θ_{c} is from $45°$ to $180°$. The contact angle is determined by fitting a circle to a cross section of the gas–liquid interface which is defined as the surface that has a density approximately half of the bulk density of the droplet. The simulated results in Figure 2c agree well with the values in Reference 43.
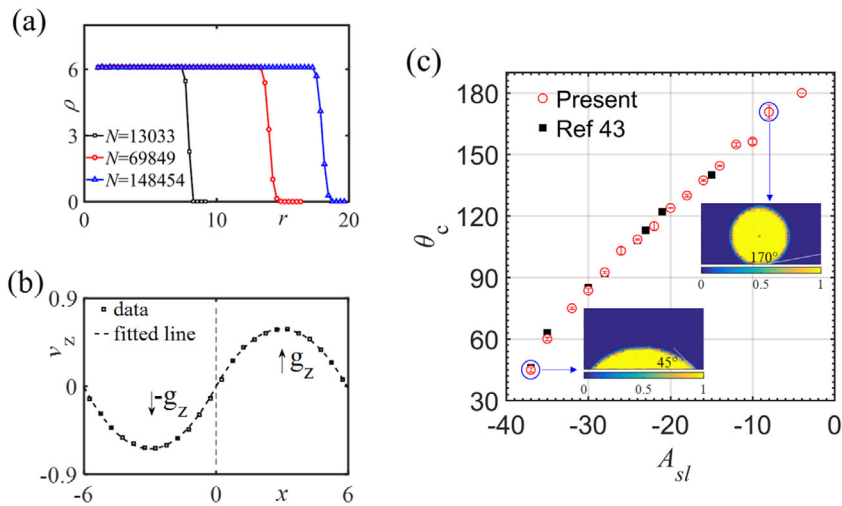
FIGURE 2 Simulation validation (a) Radial density profile of the droplet (b) Velocity profile for periodic Poiseuille flow to calculate viscosity (c) Relationship between the solid–liquid interaction parameter A_{sl} and the static contact angle θ_c. An error bar represents one standard deviation [Color figure can be viewed at wileyonlinelibrary.com]

For further validation, we now consider the case of an impacting droplet for which experimental data is available (Reference 39). The time evolution of the impacting droplet with $We = 12.1$ in terms of its dimensionless height $H^* = H/D_0$ and spreading factor $D^* = D/D_0$ with D_0 the initial droplet diameter is shown in Figure 3. The maximum spreading factor (D^*_{max}) and the spreading time (from the impact to the maximum spread) are 1.57 and 9.2 μs, corresponding to the value 1.4 ± 0.2 and 9.2 ± 2.2 μs in the reference.[39] Finally, the droplet reaches a stable state and the contact angle reaches 90°. It should be noted that we consider the surfaces as ideal. The presence of contact angle hysteresis on real surfaces can lead to a retraction of the droplet in an experiment.[24,44] After the comparison between the simulation and experimental values, we feel confident to use the MDPD method to predict droplet spreading on heterogeneous substrates.

2.3 | Problem specifications

The schematic for a droplet deposition on the periodically stripe-patterned substrate is shown in Figure 4. Here the hydrophobic stripe width equals to the hydrophilic stripe width, represented by W_s. The ratio of stripe width W_s over initial droplet diameter D_0 is defined as β. It is in the range 0.5–1.0, so that in this work the droplet is in the Beyond–Cassie–Baxter regime.[18] First we ignore the inertial effect and study the droplet wetting behavior as the droplet deposits starting from three different positions (the middle of the hydrophobic stripe—Case1; the middle of the hydrophilic stripe—Case2; and exactly the border between two different stripes—Case3), seen as Figure 4a–c. Then we choose Case 3 as an example to study inertial droplet impingement and splitting behavior on the single-striped surface and multi-striped surface.

A computational domain of size $160 \times 100 \times 60$ is adopted in the three-dimensional simulation with periodic boundary condition in the x and y directions. The x direction is normal to the stripes and y direction is in the direction of the stripes. The z direction is the direction normal to the substrate. Each droplet has diameter $D_0 = 28$ and consists of 69,849 MDPD particles ($\rho = 6.09$, $\sigma = 7.51$ and
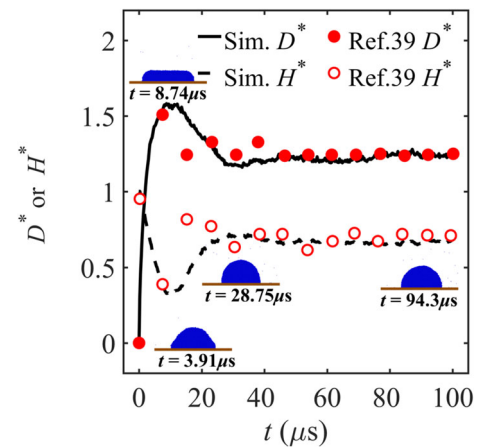

FIGURE 3 Simulation validation of time evolution of droplet dimensionless height H^* and dimensionless diameter D^* against experimental data reported in Reference 39 [Color figure can be viewed at wileyonlinelibrary.com]

$\upsilon = 0.80$ [$\gamma = 1$]), and the droplet matches the liquid with $\rho^* = 1{,}056$ kg/m³, $\sigma^* = 56.5$ mN/m, $\upsilon^* = 6.03 \times 10^{-6}$ m²/s, and its diameter equals to 37 μm. The substrate contains between 156,294 and 310,182 frozen MDPD particles. The bounce forward boundary condition[45] is applied to prevent liquid particles from penetrating the wall. Gravity is neglected. A standard velocity-Verlet algorithm is applied for the simulations, using the value of 0.5 for the empirical parameter.[11] The time step was set to 0.01 in MDPD units.

3 | RESULTS AND DISCUSSION

3.1 | Droplet wetting behavior without inertia

3.1.1 | The effect of deposition position

It has been reported that the droplet shape in spreading is sensitive to the deposition position when the droplet radius is of the same order

of magnitude as the stripe width.[18] Here, we deposit the droplet in three different positions by placing it close to the surface (within $1.0r_C$) with zero velocity so that the droplet spreads on the surface due to the attractive interaction between liquid and solid surface. The intrinsic contact angle of the hydrophilic stripe θ_{lic} and hydrophobic stripe θ_{bic} are 45° and 115°, respectively. The relative hydrophobicity α is 1 and β is 0.5.

Figure 5 shows the droplet wetting process in terms of time evolutions; snapshots are shown in Figure 6. Dimensionless scales W^* and L^* are introduced to describe the droplet morphology, defined as the width and the length of droplet divided by the droplet initial diameter D_0, respectively. At the beginning of the wetting process, until

W^* reaches 0.5, the droplet spreads isotropically with the same spreading rate in Case 1 and Case 2 (Figure 6, t = 10) since the droplet is spreading on a homogeneous part of the surface. At the moment when reaching W^* = 0.5, the droplet in Case 1 reaches the hydrophilic part of the surface and spreads faster in the x-direction as compared to the y-direction. The opposite occurs in Case 2 where the droplet has a preference to stay on the hydrophilic stripe it was deposited on. Case 2 also has a recoiling stage with the droplet retracing in the x-direction after $t \approx 100$ so as to reach a larger contact angle $\theta_\perp$ normal to the stripes. Case 3 shows a migration of the droplet towards a hydrophilic stripe (see Figure 6c) and then evolves in a way similar to Case 2 (compare Figure 5b,c).

FIGURE 4 Schematic illustration of droplet deposition on (a) the middle of hydrophobic stripe (Case 1) (b) the middle of hydrophilic stripe (Case 2) (c) the border between two different stripes (Case 3). The hydrophobic stripe width equals to hydrophilic stripe width, represented by W_s [Color figure can be viewed at wileyonlinelibrary.com]
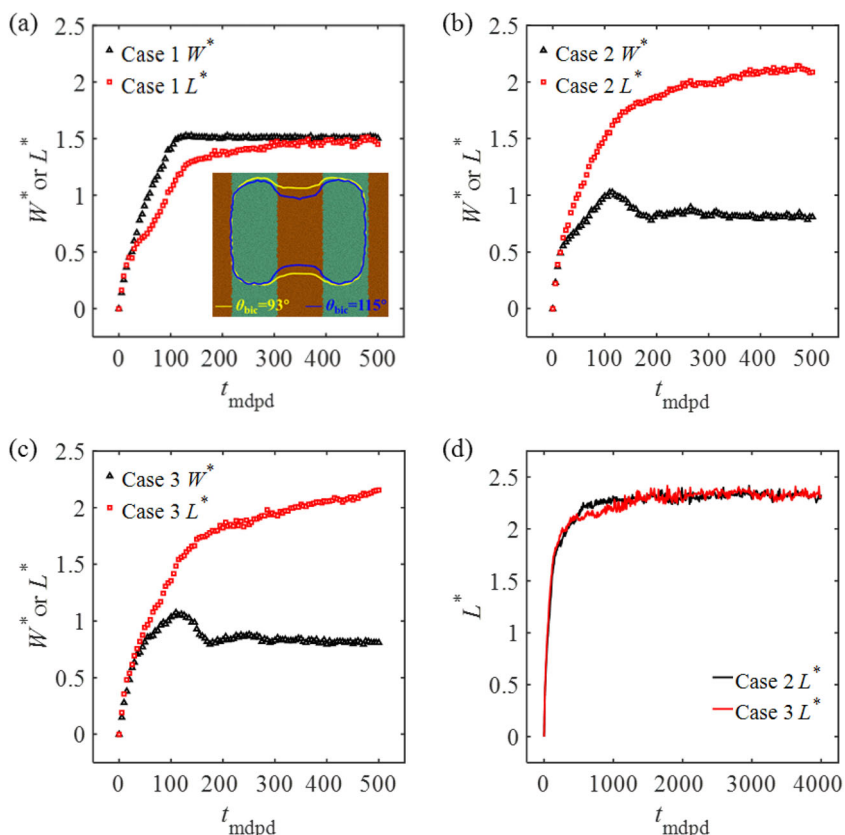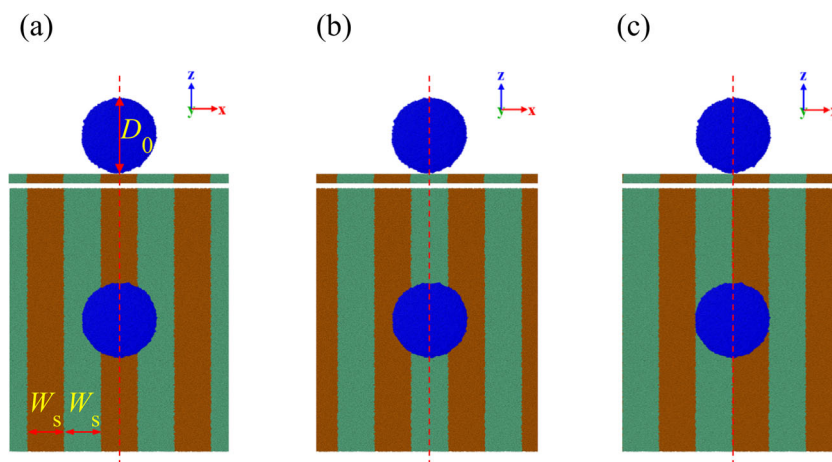

FIGURE 5 Evolution of droplet dimensionless width W^* (W^* = W/D_0) and length L^* (L^* = L/D_0) in (a) Case 1, (b) Case 2 and (c) Case 3. (d) Evolution of L^* in Case 2 and Case 3 for a longer time. The inset in (a) shows the outline of "butterfly" shape as the θ_{bic} are 93° (yellow line) and 115° (blue line), respectively [Color figure can be viewed at wileyonlinelibrary.com]
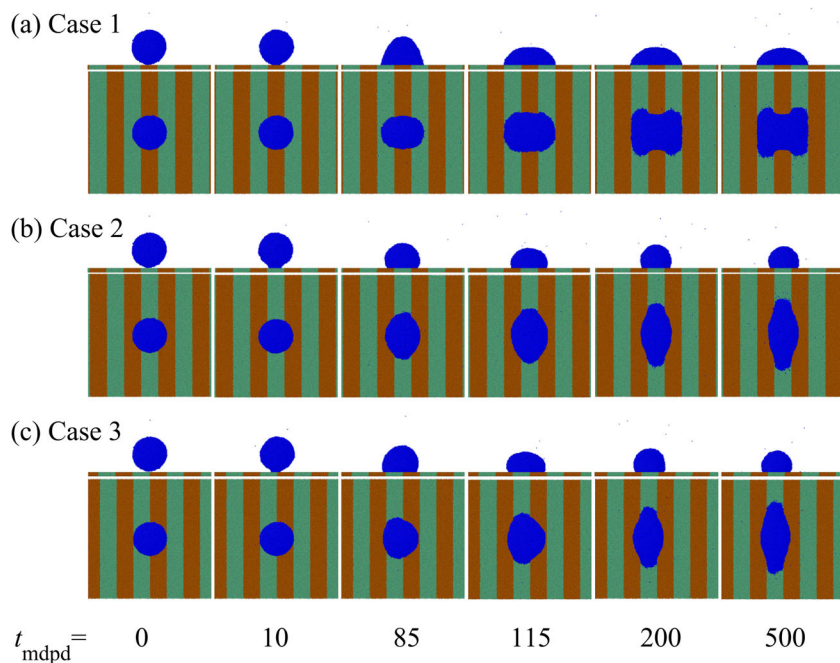
(a) Case 1

(b) Case 2

(c) Case 3

$t_{mdpd} =$ 0   10   85   115   200   500

The energy barrier in perpendicular direction to the stripe causes the droplet spreading along the stripe and a lozenge shape droplet forms in Cases 2 and 3 (Figure 6b,c, t = 500). Differently, a butterfly-like droplet with a width equal to 1.5 times its initial diameter forms in Case 1 (Figure 6a, t = 500), which also has been observed in experiments.[18] Interestingly, the droplet length and width are almost unchanged if the wettability of the hydrophobic stripe changes in Case 1 (inset in Figure 5a). The length of the neck, however, is sensitive to the wettability of the hydrophobic stripe.

3.1.2 | The effect of the wettability of the hydrophobic stripes

We now focus on the equilibrium shape of a droplet that is released—still without inertia—on the border between a hydrophobic and hydrophilic stripe. As shown in Figure 6 (Case 3), the droplet will migrate to the hydrophilic stripe. We study the effects of the droplet size relative to the stripe width (β in the range 1.0–0.5) and the wettability of the hydrophobic stripes with θ_{bic} in the range 93°–180°, while keeping fixed θ_{lic} = 45°. The variation in θ_{bic} is achieved by changing A_{bic}. Results of the simulations have been summarized in terms of the parallel and perpendicular contact angles ($\theta_{\parallel}$ and $\theta_{\perp}$, respectively) in Figure 7, and in terms of the droplet's aspect ratio in Figure 8.

In all cases, the footprint of the droplet extended over the entire width of the hydrophilic stripe, while not covering the hydrophobic stripe, see Figure 7b for two typical droplet shapes. The largest droplets—relative to the stripe width—are the ones with β = 0.5. As shown in Figure 7a, with increasing hydrophobicity initially their $\theta_{\perp}$ closely follows θ_{bic} and then levels off to $\theta_{\perp} \approx 135°$. For smaller droplets, the dependency of $\theta_{\perp}$ with A_{bic} is much weaker. If $\beta \geq 0.7$, $\theta_{\perp}$ hardly depends on the hydrophobicity. Given that $\theta_{\parallel}$ is formed on the

hydrophilic stripe, it matches closely with θ_{lic} that was set at 45°. Slight variations in $\theta_{\parallel}$ are due to uncertainties in estimating this angle. Given the shape of the droplet in the parallel direction we cannot estimate this angle via a circle fit. Therefore, we extract a part of the boundary points near the surface (up to 0.3 times the initial drop diameter above the surface) and connect those points with a polynomial curve of fourth order (red curves in Figure 7c). The contact angle is derived from the slope of the polynomial at the surface.

Figure 8 shows the aspect ratio of equilibrium droplet as a function of β and θ_{bic}. As we saw in Figure 7a, the shape of the droplet—now in terms of its aspect ratio—only depends on β for sufficiently high hydrophobicity, that is, for $\theta_{bic} \geq 155°$. It is interesting to note that for lower θ_{bic} the aspect ratio as a function of β goes through a maximum.

3.2 | Droplet impingement behavior considering inertial effect

3.2.1 | Droplet impingement on single stripe surface

In this section, we consider the effect of droplet inertia on droplet morphology. In Song et al's[23] experiment, a hydrophilic surface coating with a slim superhydrophobic stripe was found performing well in splitting droplet if the Weber number (*We*) of the droplet was sufficiently high, indicating the potential of this chemically striped surface for splitting droplets in microfluidics applications. Here we investigated the droplet splitting behavior on the hydrophilic surface coated with a superhydrophobic stripe with various widths. Compared with a low β in Song et al's experiment[23] (β 0.2), β is larger in this work with the range of 0.5–1.0. The contact angles of the hydrophilic surface and the hydrophobic stripe are 45° and 170°, respectively.
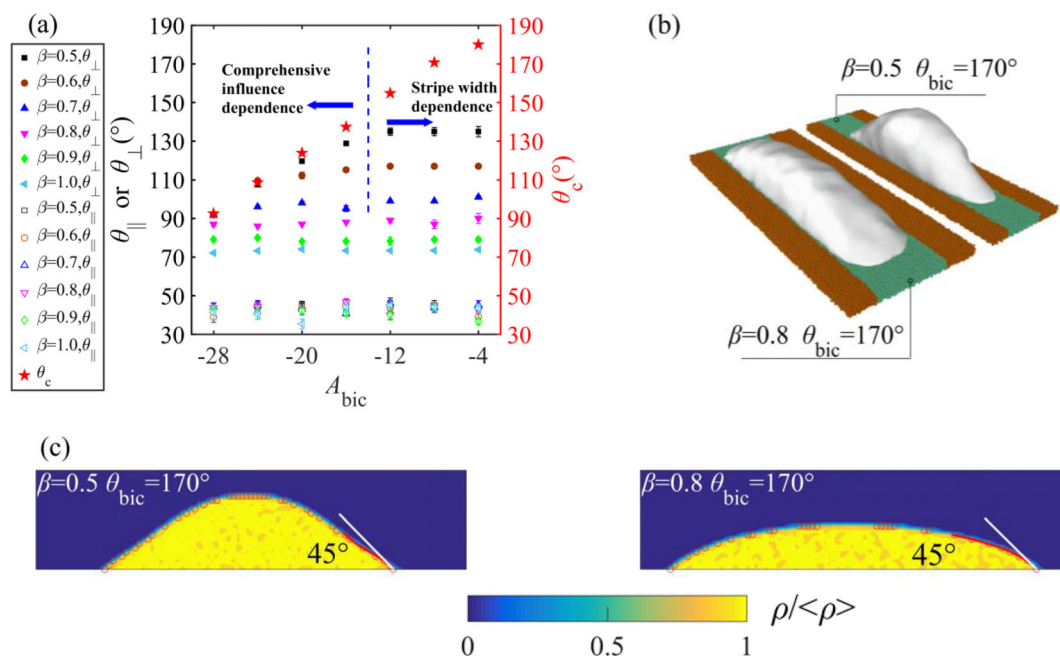
FIGURE 7 (a) $\theta_\perp$ and $\theta_\parallel$ of the droplet at its equilibrium state dependence on hydrophobic stripe wettability (A_{bic}) and β, that is, the ratio of the stripe width and initial droplet diameter, when the intrinsic contact angle of hydrophilic stripes (θ_{lic}) is fixed as $45°$. Pentagons represent the intrinsic contact angle of hydrophobic stripes (θ_{bic}) corresponding to A_{bic} derived from Figure 2c. (b) The channel like (left, $\beta = 0.5$, $\theta_{bic} = 170°$) and bulge like (right, $\beta = 0.8$, $\theta_{bic} = 170°$) shape. (c) $\theta_\parallel$ estimate example. The red curves are the polynomial fits. (see the text) [Color figure can be viewed at wileyonlinelibrary.com]
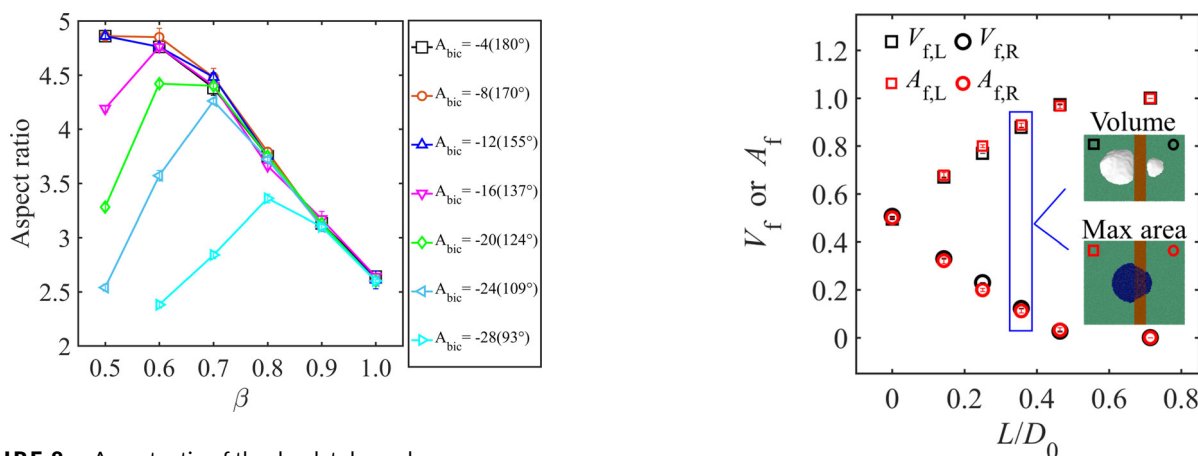

FIGURE 8 Aspect ratio of the droplet dependence on hydrophobic stripe wettability A_{bic} (θ_{bic}) and β [Color figure can be viewed at wileyonlinelibrary.com]

FIGURE 9 Split volume and maximum footprint area fractions of the droplet on two sides of a single stripe as the deposition position varies. L is the distance between droplet deposition point and the center line of the stripe. $V_{f,L} = V_L/V_0$, $V_{f,R} = V_R/V_0$, $A_{f,L} = A_L/(A_L + A_R)$, $A_{f,R} = A_R/(A_L + A_R)$, where V_L and V_R represent the left and right split droplet volume, A_L and A_R are the left and right footprint area when the droplet reaches its maximum spread on hydrophobic stripe [Color figure can be viewed at wileyonlinelibrary.com]

Taking the case $\beta = 0.5$ as an example, we investigate the effect of droplet deposition position on the volume fraction (V_f) and maximum-footprint-area fraction (A_f) of split droplets, and the results are shown in Figure 9. Note that V_f is obtained by the split droplet volume scaled to the initial droplet volume, and A_f is obtained by each part of maximum-footprint-area scaled to the total footprint-area on the hydrophilic surface. In Figure 9, we can see that V_f matches A_f, and this characteristic agrees well with that proposed by Song et al.[23] It can also be seen in Figure 9 that the difference of volume fraction between two split droplets increases approximately linearly with L/D_0

until the entire droplet ends up on one side of the stripe and no split has happened.

Taking Case 3 (as defined in Figure 4) as an example, we illustrate the asymmetric splitting behavior on a single stripe surface with β equal to 0.5 and 0.9 at We = 22.7 in Figure 10. The droplet exhibits

two equilibrium states: split off or shift to the hydrophilic area. During the impingement, the projection of the droplet remains circular as it radially spreads outwards (for $t \leq 10$), indicating that the droplet's inertia dominates the spreading process during this stage. Subsequently, the droplets behave differently due the different values of β. In the case $\beta = 0.5$, the droplet inertia (characterized by the Weber number) is high enough for the droplet to cross the superhydrophobic stripe and enter the hydrophilic area right of the stripe ($t = 10$). After reaching its maximum spreading on the superhydrophobic stripe ($t = 30$), the part of the droplet on the superhydrophobic stripe starts to get squeezed, and a liquid neck forms. From then on, the droplet keeps stretching along the direction perpendicular to the stripe. The liquid neck collapses and the droplet splits into two (at $t = 230$). In the case $\beta = 0.9$, the edge of the droplet fails to reach the hydrophilic area at the opposite side of the stripe because its inertia and associated kinetic energy is insufficient for this. After reaching the maximum spreading ($t = 30$), the edge of the droplet on the superhydrophobic stripe retracts while the liquid on the hydrophilic area still spreads outwards and the droplet becomes shell-like with a gibbous frontier on the edge (in the side view when $t = 40$). Gradually, the part of the droplet on the superhydrophobic stripe retracts back to the hydrophilic area and stays in hydrophilic area at its equilibrium state ($t \geq 230$).

The eventual droplet state is co-determined by droplet inertia and surface properties, which can be characterized by We and β as well as the contact angles of the hydrophilic surface and the hydrophobic stripe. Here we focus on the effects of We and β at fixed $\theta_{\text{bic}} = 170°$ $\theta_{\text{lic}} = 45°$. In the Appendix we show the (limited) sensitivity of these contact angles on the final droplet morphology (Figures 15 and 16) .

The effect of We and β on the droplet equilibrium shape is visualized in Figure 11a, where the red circle represent droplet split off cases. To find the critical boundary for droplet split-off, we did additional simulations of droplet impingent on a homogeneous superhydrophobic surface over a range of We with a fixed superhydrophobic contact angle of 170°. For convenience, we introduce the maximum spreading radius factor, $R_{\max}^*$, defined as the maximum value of R^* (the ratio between droplet spreading radius and D_0). The history of R^* is shown in Figure 11c. We find that initially R^* increases with time and then decreases after reaching the peak. Given that—mostly—the peak in radius is not very sharp, we take an average over a few data points around the peak values to determine $R_{\max}^*$ as indicated in Figure 11c. The relationship between $R_{\max}^*$ and We is plotted in Figure 11a,b, as black squares.

Coming back to droplet deposition on a single-stripe surface, at a specific Weber number, the droplet splits if $R_{\max}^* > \beta$, whereas
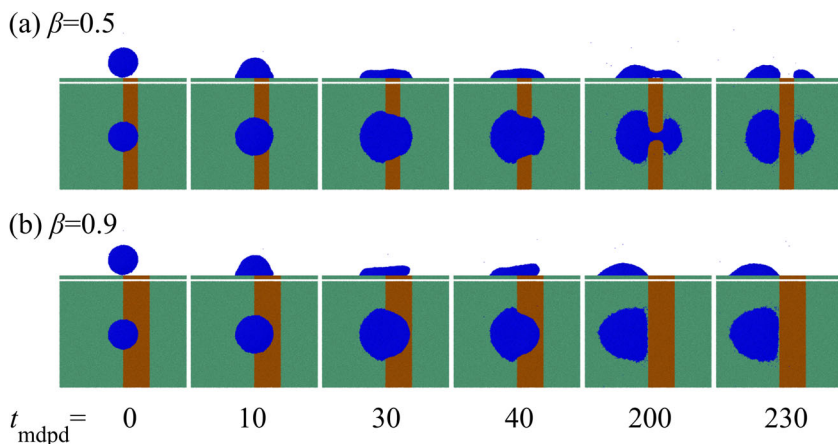

FIGURE 10 Evolution of impinging droplet with Weber number (We) equals 22.7 on single-stripe-patterned surface [Color figure can be viewed at wileyonlinelibrary.com]
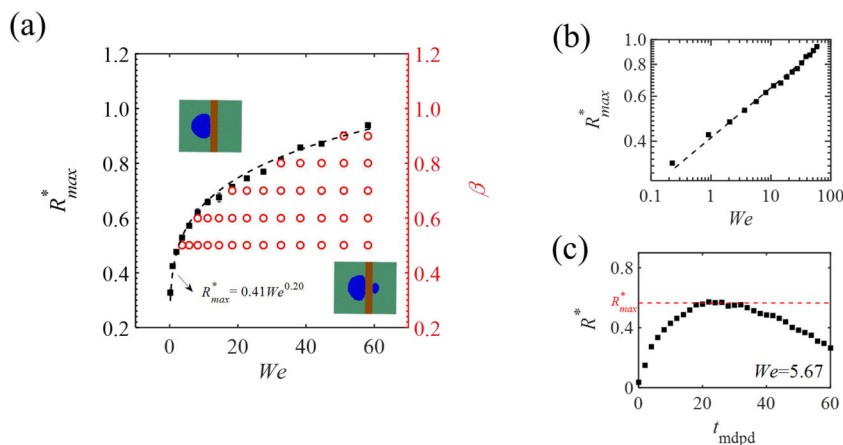

FIGURE 11 (a) Determination of droplet split in a single-stripe system. The hollow circle signed the cases droplet split off, where $R_{\max}^* > \beta$ under the same We. The black solid squares represent $R_{\max}^*$ versus We. (b) the logarithmic scale of $R_{\max}^*$ versus We and they are the same as in the figure(a). (c) Time history of R^* [Color figure can be viewed at wileyonlinelibrary.com]

otherwise it will shift to the hydrophilic side. It implies that the hydrophilic surface with a superhydrophobic stripe has the capability to split the droplet as long as the droplet can get across the stripe at its maximum spreading.

Therefore, the concept of R_{max}^* can help us to predict the result of droplet impingement: splitting off or a shift to hydrophilic side. Power law behavior of $R_{max}^* \propto We^{\alpha_1}$ has been proposed based on theoretical analysis.[46] A scaling law of $R_{max}^* \propto We^{0.5}$ has been found by a balance between inertia and surface tension forces when We is large enough and viscous energy dissipation is neglected.[47,48] On the other hand, Clanet et al[49] regarded the maximum droplet shape as a balance between gravity and surface forces. They determined the droplet thickness at maximum spread based on capillary length and obtained $R_{max}^* \propto We^{0.25}$ by imposing volume conservation. Recently, Lin et al[46] found the above exponents in scaling law also related to the viscosity of the droplet in their experiments, where α_1 can be as high as 0.25 for water, and as low as 0.1 for a 397.8 mPa·s viscous liquid. Based on our simulations, we found $R_{max}^* \propto We^{0.20}$, see Figure 11b.

3.2.2 | Droplet impingement on periodically hydrophilic and hydrophobic stripes

Now, we investigate droplet splitting behavior on a periodic multi-striped surface. The deposition point and the contact angles are unchanged. The value of We has been fixed at 22.7, so that the droplet splits when $\beta \leq 0.75$ on a single-striped surface, as shown in Figure 11. However, we find the droplet exhibits a "butterfly" shape on multi-striped surface if $\beta = 0.5$ (Figure 12a, $t = 675$), indicating the influence of the multi-striped mode on the eventual droplet state.

Figure 12 shows more details about an impinging droplet on multi-striped surfaces with various β. Initially ($t \leq 10$), the droplet sets

in the spreading stage, where the droplet inertia dominates the evolution process so that the droplet spreads outwards with the same speed in all three cases. Subsequently, the droplet behaves differently for different β. For $\beta = 0.5$, the liquid on the superhydrophobic stripes retracts when $t \geq 30$. During this retracting process, the gibbous part of the droplet on hydrophobic stripes prefers to move directly to the hydrophilic stripes, while the liquid on the right hydrophilic stripe is still stretching outwards until it fills up the entire width of the hydrophilic stripe (Figure 12a, $\beta = 0.5$, $t = 100$). The droplet neck forms during droplet recoiling. However, compared to the spreading behavior on a single-striped surface, more liquid is contained in the droplet neck on a multi-striped surface. This results in the deceleration of the neck-shrink, as illustrated in Figure 12a. Finally, the droplet remains intact after impingement and becomes "butterfly" shape.

For cases with larger β, there is enough space on the right hydrophilic stripe for liquid to stretch and spread radially, generating the collapse of the neck and finally droplet split-off (Figure 12b, $\beta = 0.7$, $t = 175$). In addition, the periodic chemical stripes reshape the split droplet to an elongated shape. If the stripe is wide enough so as to hinder the droplet stepping over the superhydrophobic stripe, the droplet will vibrate on the hydrophilic stripe until it consumes the remaining energy. Finally, the droplet exhibits an elongated shape without any splitting, as revealed in Figure 12c.

The aforementioned droplet behavior on a multi-striped surface can be quantitatively described by analyzing the energy associated to the droplet. The conversion of energy during the process of droplet impingement on the substrate can be expressed as

$$E_k^0 + E_s^0 + A_{sv}\sigma_{sv} = A_{lv}\sigma_{lv} + A_{ls}\sigma_{ls} + (A_{sv} - A_{ls})\sigma_{sv} + E_k + E_v, \quad (5)$$

where, E_k^0 and E_s^0 denote the droplet initial kinetic energy and surface energy, respectively. A_{sv}, A_{lv} and A_{ls} represent the area of solid-vapor surface, liquid–vapor surface and liquid–solid surface, and their
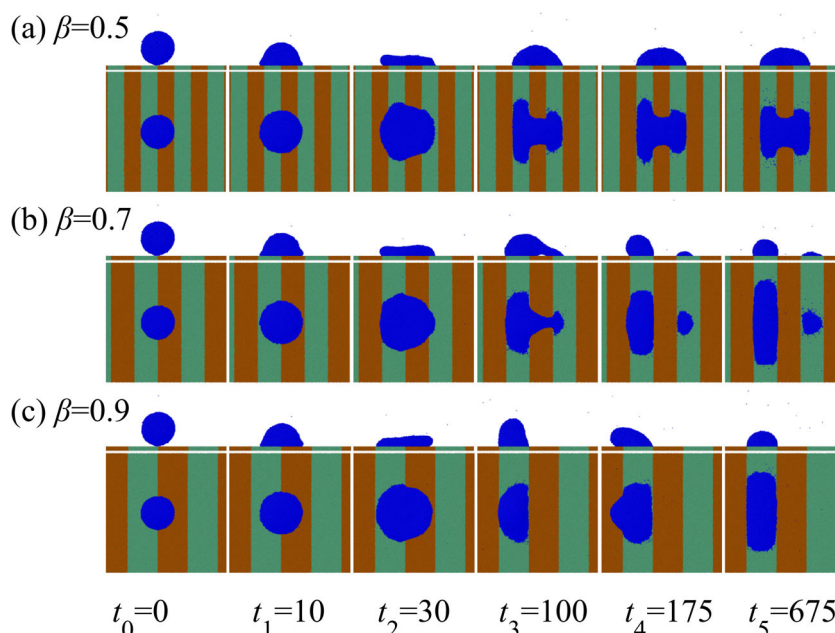

FIGURE 12 Temporal of impinging droplet with $We = 22.7$ on different β surface. The time is in MDPD units. MDPD, many-body dissipative particle dynamics [Color figure can be viewed at wileyonlinelibrary.com]

corresponding surface tension are σ_{sv}, σ_{lv}, and σ_{ls}. Clearly, the interfacial energy of solid-vapor surface can be removed on the both side of the equation. Therefore, we have:

$$E_s^0 + E_k^0 = E_s + E_k + E_v, \tag{6}$$

where

$$E_s = A_{lv}\sigma_{lv} + A_{ls}(\sigma_{ls} - \sigma_{sv}) \tag{7}$$

From the Young's equation we know that $\sigma_{ls} - \sigma_{sv} = -\sigma_{lv}\cos\theta_c$. Hence,

$$E_s = A_{lv}\sigma_{lv} - A_{ls,bic}\sigma_{lv}\cos\theta_{bic} - A_{ls,lic}\sigma_{lv}\cos\theta_{lic} \tag{8}$$

where $A_{ls,bic}$ and $A_{ls,lic}$ are the area of liquid–solid surface on the hydrophobic stripes and hydrophilic stripes, respectively.
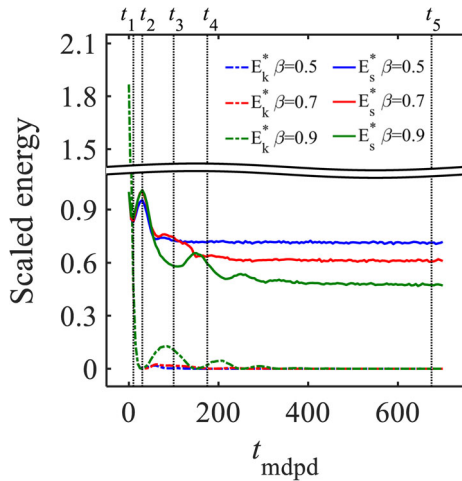

FIGURE 13 The scaled surface energy and kinetic energy of the droplet as a function of time for different β surface. *We* fixed at 22.7, and the time t_1, t_2, t_3, t_4, t_5 referred back to Figure 12 [Color figure can be viewed at wileyonlinelibrary.com]

E_k can be calculated by

$$\vec{v}_{mean} = \frac{1}{N}\sum_{i=1}^{N}\vec{v}_i \tag{9}$$

$$E_k = \frac{1}{2}M|\vec{v}_{mean}|^2 = \frac{1}{2}M\left(v_{x,mean}^2 + v_{y,mean}^2 + v_{z,mean}^2\right)$$

where v_x, v_y, v_z are the velocity components of each particle and M is the droplet mass, that is, the number of liquid particles since each particle mass equals to 1. The normalized kinetic energy (E_k^*) and surface energy (E_s^*) are obtained by E_k/E_s^0 and E_s/E_s^0, respectively. The viscous dissipation energy E_v is related to the droplet viscosity and velocity.

Figure 13 shows the time history of the scaled energy E_k^* and E_s^*. At the beginning of deposition ($t \leq 10$), the spreading droplet has a nearly spherical cap shape. The loss rate of E_k^* is more than the loss rate of E_s^*. Then the droplet starts spreading asymmetrically, where E_k^* still decreases while E_s^* rises slightly. We note that E_s^* reaches its local maximum when E_k^* reduces to zero (at $t = 30$), and there E_s^* ($\beta = 0.9$) $\approx E_s^*$ ($\beta = 0.7$) > E_s^* ($\beta = 0.5$). However, the droplet does not come to a halt; surface energy starts to convert into kinetic energy. The droplet now is in an energy fluctuation stage. The fluctuation of E_s^* and E_k^* is gentle for $\beta = 0.5$ and more violent for $\beta = 0.9$ before the droplet reaches equilibrium. The fluctuations relate to the morphologic changes in Figure 12. Finally, the droplet comes to rest when $t > 500$. In addition, E_s^* and E_k^* are stable. We can see that E_s^* ($\beta = 0.5$) > E_s^* ($\beta = 0.7$) > E_s^* ($\beta = 0.9$) in steady state, indicating that smaller β helps forming droplets with higher surface energy.

Figure 14a illustrates that *We* and β affect the eventual droplet shape simultaneously. Clearly, small *We* and large β tend to make the droplet elongated on the stripe. This is because lower kinetic energy cannot sufficiently help the droplet overcome the energy barrier formed by the superhydrophobic stripes, which results in the droplet retracting and spreading along the hydrophilic stripe. The equilibrium shape of the droplet generally changes from elongated to split as *We* increases. The critical boundary, expressed by R_{max}^* in single-striped cases, is also valid for multi-striped cases. Generally, droplets split if
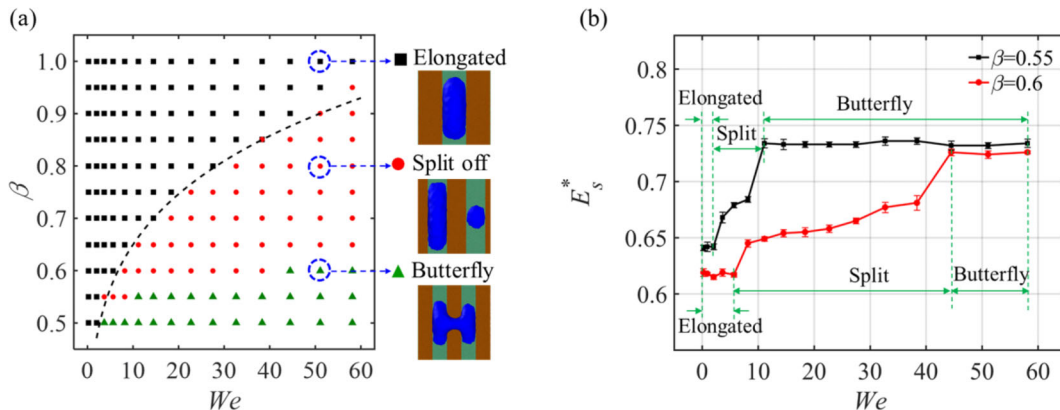

FIGURE 14 (a) Droplet morphology as a function of *We* and β. The dot line represents the relationship of *We* and R_{max}^* derived from Figure 11a for single stripe system. (b) the scaled surface energy E_s^* as a function of *We* [Color figure can be viewed at wileyonlinelibrary.com]

$R_{max}^* > \beta$. However, the "butterfly" shape occurs if $\beta \le 0.6$. In addition, there is a mixed regime where elongated or split droplets occur randomly. This is when β is near the maximum spreading radius factor R_{max}^* (dotted line in Figure 14a).

Figure 14b shows E_s^* as a function of We for two different β cases. Clearly, the droplet transforms from low surface energy (elongated shape) to high energy (split-off or even "butterfly" shape) as We increases. The value of E_s^* remains constant when the droplet is elongated or has a "butterfly" shape. For the "butterfly" shape, there is little difference in E_s^* between the two β cases. For the elongated shape, however, E_s^* is much lower in the higher β case, which means more energy is required to transform the droplet state from elongated to butterfly for higher β.

The chemically multi-striped surface is found to transform the droplet into three morphologies when droplet inertia is considered. The diagram for the droplet morphology may be used in microfluidic system to control droplet shape or split the droplet. It should be noted that the droplet morphology only depends on β and not on We if the droplet is elongated or "butterfly" shaped since the surface energy
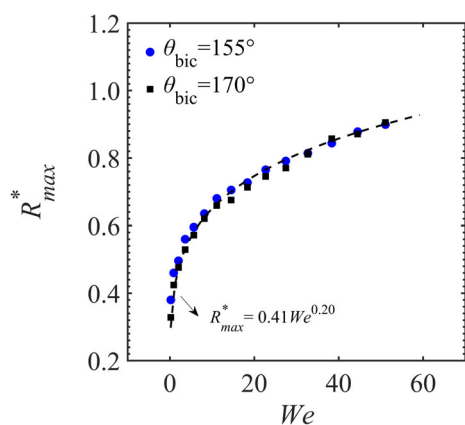
stays constant, as shown in Figure 14b. When the droplet is split, one can get a desired split by adjusting β and We.

As stated above, the results presented in this section are for $\theta_{bic} = 170°$ and $\theta_{lic} = 45°$. In the Appendix the sensitivity of the contact angles has been investigated. Additionally, it should be emphasized that the surfaces in our simulation are smooth since we focus on the effect of contact angle difference between superhydrophobic and hydrophilic stripe on droplet morphology. However, experiment is surface roughness, especially for superhydrophobic surfaces that are usually decorated by micro−/nanostructures.

4 | CONCLUSIONS

In this work, three-dimensional MDPD simulation was employed to investigate the droplet impingement and subsequent wetting behavior on chemically stripe-patterned surfaces with β (which is the ratio of stripe width over droplet diameter) ranging from 0.5 to 1.0. Two scenarios, with and without inertial effects, were explored.

To validate the MDPD method in describing the droplet impingement behavior on solid surfaces, we firstly matched the physical properties of a given liquid with the dimensionless MDPD system. Then comparison between the simulation and experimental results showed the ability of MDPD in properly simulating droplet impingement behavior.

Subsequently, we investigated the droplet wetting behavior without inertial effects on striped surfaces. We found that a recoiling stage was only present when the droplet deposited on the middle of a hydrophilic stripe or on the border of the stripe. The latter case was studied more extensively. We found that the parallel contact angle was constant and was close to the intrinsic contact angle on the hydrophilic stripes. On the other hand, when the hydrophobic stripes are superhydrophobic, the perpendicular contact angle and aspect ratio of the droplet only depend on β.

As for the case with inertial effects, droplet impingement behavior on single-striped surfaces and on multi-striped surfaces were both
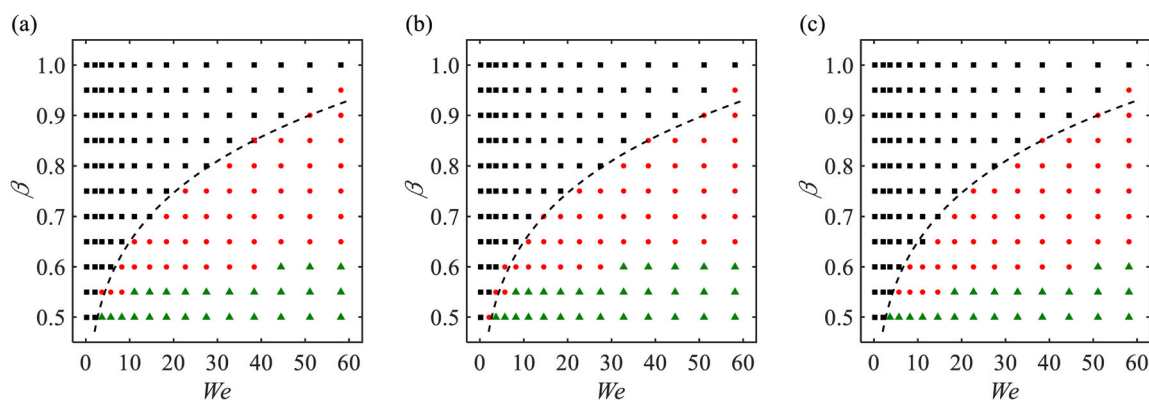
FIGURE 15 The relationship between R_{max}^* and We on homogenous surface with different intrinsic contact angle θ_{bic} [Color figure can be viewed at wileyonlinelibrary.com]

FIGURE 16 Droplet morphology on multi-striped surface with (a) $\theta_{bic} = 170°$ $\theta_{lic} = 45°$ (b) $\theta_{bic} = 155°$ $\theta_{lic} = 45°$ (c) $\theta_{bic} = 170°$ $\theta_{lic} = 60°$. The dotted lines in these three figures are the same, and its expression is $R_{max}^* = 0.41We^{0.20}$. The color coding is the same as in Figure 14 [Color figure can be viewed at wileyonlinelibrary.com]

investigated, where the contact angle θ_{bic} is larger than 150°. For single-striped surfaces, the droplet splits into two with the distribution of volume approximately equal to the maximum-footprint-area distribution. The Weber number (We) affects the droplet morphology and the critical condition for droplet split-off is identified as $R^*_{max} = 0.41We^{0.20}$ where the droplet splits when $R^*_{max} > \beta$. Different from impinging on single-striped surfaces, three droplet morphologies, elongated, split off and "butterfly" shape, were observed on multi-striped surfaces. Both We and β affect the droplet morphology. A droplet splits for high We and low β, while "butterfly" droplet occurs if β is less than or equal to 0.6. The critical condition $R^*_{max} = 0.41We^{0.20}$ is also valid to predict the droplet morphology on multi-striped surfaces with elongated droplets if $R^*_{max} < \beta$. It was also shown—see the Appendix—that this criterion is not sensitive to the specific values of θ_{bic} and θ_{lic}.

Finally, through the analysis of the scaled surface energy of the droplet, we found that β is the only factor affecting the shape of elongated and "butterfly" droplets. Overall, the current study provides the potential of precise control of droplet morphology in the Beyond–Cassie–Baxter regime by modifying the parameter β, stripe wettability and We. It could help support the design of microfluidic devices where the droplet morphology needs careful control.

Non-Newtonian liquid droplets are widely used in the applications such as inkjet printing[50] and bioprinting.[51] Different from New-tonian fluid, the viscosity of non-Newtonian fluid is strongly dependent on the applied stress. Considering the special behavior of non-Newtonian fluid is therefore of practical as well as of academic interest. We will be working on the spreading of such liquid droplet in the Beyond–Cassie–Baxter regime in future research.

ORCID

Jos J. Derksen https://orcid.org/0000-0002-9813-356X

REFERENCES

1. Chen Y, He B, Lee J, Patankar NA. Anisotropy in the wetting of rough surfaces. *J Colloid Interface Sci*. 2005;281:458-464.
2. Semprebon C, Mistura G, Orlandini E, Bissacco G, Segato A, Yeomans JM. Anisotropy of water droplets on single rectangular posts. *Langmuir*. 2009;25:5619-5625.
3. Yao X, Song Y, Jiang L. Applications of bio-inspired special wettable surfaces. *Adv Mater*. 2011;23:719-734.
4. Wu L, Dong Z, Kuang M, et al. Printing patterned fine 3D structures by manipulating the three phase contact line. *Adv Funct Mater*. 2015; 25:2237-2242.
5. Shang X, Luo Z, Bai B. Droplets trapped by a wetting surface with chemical defects in shear flows. *Chem Eng Sci*. 2019;195: 433-441.
6. Jansen HP, Zandvliet HJW, Kooij ES. Evaporation of elongated droplets on chemically stripe-patterned surfaces. *Int J Heat Mass Transf*. 2015;82:537-544.
7. Macis M, Lugli F, Zerbetto F. Modeling living cells response to surface tension and chemical patterns. *ACS Appl Mater Interfaces*. 2017;9: 19552-19561.
8. Patrick Jansen H, Sotthewes K, Zandvliet HJW, Kooij ES. Potential of lattice Boltzmann to model droplets on chemically stripe-patterned substrates. *Appl Surf Sci*. 2016;361:122-132.
9. Wu Y, Wang F, Selzer M, Nestler B. Investigation of equilibrium droplet shapes on chemically striped patterned surfaces using phase-field method. *Langmuir*. 2019;35:8500-8516.
10. Zou L, Wang H, Zhu X, Chen R, Ding Y, Liao Q. Maximum spread of droplets on chemically striped surfaces. *AIChE J*. 2019;66:e16774.
11. Varagnolo S, Schiocchet V, Ferraro D, et al. Tuning drop motion by chemical patterning of surfaces. *Langmuir*. 2014;30:2401-2409.
12. Carmeliet J, Chen L, Kang Q, Derome D. Beyond-Cassie mode of wetting and local contact angles of droplets on checkboard-patterned surfaces. *Langmuir*. 2017;33:6192-6200.
13. Lin C, Chen S, Xiao L, Liu Y. Tuning drop motion by chemical chessboard-patterned surfaces: a many-body dissipative particle dynamics study. *Langmuir*. 2018;34:2708-2715.
14. Bliznyuk O, Vereshchagina E, Kooij ES, Poelsema B. Scaling of anisotropic droplet shapes on chemically stripe-patterned surfaces. *Phys Rev E*. 2009;79:041601.
15. Damle VG, Rykaczewski K. Nano-striped chemically anisotropic surfaces have near isotropic wettability. *Appl Phys Lett*. 2017;110: 171603.
16. Bliznyuk O, Jansen HP, Kooij ES, Poelsema B. Initial spreading kinetics of high-viscosity droplets on anisotropic surfaces. *Langmuir*. 2010;26: 6328-6334.
17. Jansen HP, Bliznyuk O, Kooij ES, Poelsema B, Zandvliet HJW. Simulating anisotropic droplet shapes on chemically striped patterned surfaces. *Langmuir*. 2011;28:499-505.
18. Wang Y, Jian M, Liu H, Zhang X. Anisotropic Wetting of droplets on stripe-patterned chemically heterogeneous surfaces: effect of length ratio and deposition position. *Langmuir*. 2018;35:4387–4396.
19. Jansen HP, Sotthewes K, Ganser C, Zandvliet HJW, Teichert C, Kooij ES. Shape of picoliter droplets on chemically striped patterned substrates. *Langmuir*. 2014;30:11574-11581.
20. Léopoldès J, Dupuis A, Bucknall DG, Yeomans JM. Jetting micron-scale droplets onto chemically heterogeneous surfaces. *Langmuir*. 2003;19:9818-9822.
21. Brinkmann M, Lipowsky R. Wetting morphologies on substrates with striped surface domains. *J Appl Phys*. 2002;92:4296-4306.
22. Lipowsky R, Brinkmann M, Dimova R, Franke T, Kierfeld J, Zhang X. Droplets, bubbles, and vesicles at chemically structured surfaces. *J Phys Condens Matter*. 2005;17:S537-S558.
23. Song D, Song B, Hu H, Du X, Zhou F. Selectively splitting a droplet using superhydrophobic stripes on hydrophilic surfaces. *Phys Chem Chem Phys*. 2015;17:13800-13803.
24. Zhao J, Chen S, Liu Y. Dynamical behaviors of droplet impingement and spreading on chemically heterogeneous surfaces. *Appl Surf Sci*. 2017;400:515-523.
25. Jansen HP, Sotthewes K, Ganser C, Teichert C, Zandvliet HJW, Kooij ES. Tuning kinetics to control droplet shapes on chemically striped patterned surfaces. *Langmuir*. 2012;28:13137-13142.
26. Wang Y, Shangguan Q, Zhang D. Many-body dissipative particle dynamics simulation of the anisotropic effect of droplet wetting on stripe-patterned heterogeneous surfaces. *Appl Surf Sci*. 2019;494: 675-683.
27. Zou L, Wang H, Zhu X, Ding Y, Chen R, Liao Q. Droplet splitting on chemically striped surface. *Colloids Surf A Physicochem Eng Asp*. 2018; 537:139-148.

28. Cupelli C, Henrich B, Glatzel T, Zengerle R, Moseler M, Santer M. Dynamic capillary wetting studied with dissipative particle dynamics. *New J Phys*. 2008;10:043009.

29. Liang Y-E, Weng Y-H, Hsieh IF, Tsao H-K, Sheng Y-J. Attractive encounter of a nanodrop toward a nanoprotrusion. *J Phys Chem C*. 2017;121:7923-7930.

30. Zhao J, Chen S, Liu Y. Spontaneous wetting transition of droplet coalescence on immersed micropillared surfaces. *App Math Model*. 2018; 63:390-404.

31. Zhang K, Li Z, Maxey M, Chen S, Karniadakis GE. Self-cleaning of hydrophobic rough surfaces by coalescence-induced wetting transition. *Langmuir*. 2019;35:2431-2442.

32. Wu C-J, Chu K-C, Sheng Y-J, Tsao H-K. Sliding dynamic behavior of a nanobubble on a surface. *J Phys Chem C*. 2017;121:17932-17940.

33. Plimpton S. Fast parallel algorithms for short-range molecular dynamics. *J Comput Phys*. 1995;117:1-19.

34. Warren PB. Vapor-liquid coexistence in many-body dissipative particle dynamics. *Phys Rev E*. 2003;68:066702.

35. Español P, Warren PB. Perspective: dissipative particle dynamics. *J Chem Phys*. 2017;146:150901.

36. Hoogerbrugge PJ, Koelman JMVA. Simulating microscopic hydrodynamic phenomena with dissipative particle dynamics. *Europhys Lett*. 1992;19:155-160.

37. Arienti M, Pan W, Li X, Karniadakis G. Many-body dissipative particle dynamics simulation of liquid/vapor and liquid/solid interactions. *J Chem Phys*. 2011;134:204114.

38. Español P, Warren PB. Statistical mechanics of dissipative particle dynamics. *Europhys Lett*. 1995;30:191-196.

39. Son Y, Kim C. Spreading of inkjet droplet of non-Newtonian fluid on solid surface with controlled contact angle at low Weber and Reynolds numbers. *J Non-Newton Fluid Mech*. 2009;162:78-87.

40. Vázquez UOM, Shinoda W, Moore PB, Chiu C-C, Nielsen SO. Calculating the surface tension between a flat solid and a liquid: a theoretical and computer simulation study of three topologically different methods. *J Math Chem*. 2008;45:161-174.

41. Backer JA, Lowe CP, Hoefsloot HC, Iedema PD. Poiseuille flow to measure the viscosity of particle model fluids. *J Chem Phys*. 2005; 122:154503.

42. Boromand A, Jamali S, Maia JM. Viscosity measurement techniques in dissipative particle dynamics. *Comput Phys Commun*. 2015;196:149-160.

43. Weng Y-H, Liang Y-E, Sheng Y-J, Tsao H-K. Controlling nanodrop passage through capillary nanovalves by adjusting lyophilic crevice structure. *J Phys Chem C*. 2018;122:2231-2237.

44. Ashoke Raman K, Jaiman RK, Lee Y-S, Low H-T. Dynamics of simultaneously impinging drops on a dry surface: role of impact velocity and air inertia. *J Colloid Interface Sci*. 2017;486:265-276.

45. Ahmadlouydarab M, Hemeda AA, Ma Y. Six stages of microdroplet detachment from microscale fibers. *Langmuir*. 2018;34:198-204.

46. Lin S, Zhao B, Zou S, Guo J, Wei Z, Chen L. Impact of viscous droplets on different wettable surfaces: impact phenomena, the maximum spreading factor, spreading time and post-impact oscillation. *J Colloid Interface Sci*. 2018;516:86-97.

47. Bennett T, Poulikakos D. Splat-quench solidification: estimating the maximum spreading of a droplet impacting a solid surface. *J Mater Sci*. 1993;28:963-970.

48. Eggers J, Fontelos MA, Josserand C, Zaleski S. Drop dynamics after impact on a solid wall: theory and simulations. *Phys Fluids*. 2010;22:062101.

49. Clanet C, Béguin C, Richard D, Quéré D. Maximal deformation of an impacting drop. *J Fluid Mech*. 2004;517:199-208.

50. Sarojini Kg K, Dhar P, Varughese S, Das SK. Coalescence dynamics of pedot:pss droplets impacting at offset on substrates for inkjet printing. *Langmuir*. 2016;32:5838-5851.

51. Chimene D, Peak CW, Gentry JL, et al. Nanoengineered ionic–covalent entanglement (nice) bioinks for 3d bioprinting. *ACS Appl Mater Interfaces*. 2018;10:9957-9968.

SUPPORTING INFORMATION

Additional supporting information may be found online in the Supporting Information section at the end of this article.